Post-Print

When citing this work, cite the original published paper.

Permanent link to this version
http://hdl.handle.net/11311/1026510

Validation results of satellite mock-up capturing experiment using nets

Alberto Medina[a], Lorenzo Cercós[a], Raluca M. Stefanescu[b], Riccardo Benvenuto[c], Vincenzo Pesce[c], Marco Marcon[c], Michèle Lavagna[c], Iván González[d], Nuria Rodríguez López[d], Kjetil Wormnes[e]

[a] GMV, Spain
[b] GMV, Romania
[c] Politecnico di Milano, Italy
[d] Fundación PRODINTEC, Spain
[e] European Space Agency (ESA), The Netherlands

Abstract

The PATENDER activity (Net parametric characterization and parabolic flight), funded by the European Space Agency (ESA) via its Clean Space initiative, was aiming to validate a simulation tool for designing nets for capturing space debris. This validation has been performed through a set of different experiments under microgravity conditions where a net was launched capturing and wrapping a satellite mock-up.

This paper presents the architecture of the thrown-net dynamics simulator together with the set-up of the deployment experiment and its trajectory reconstruction results on a parabolic flight (Novespace A-310, June 2015). The simulator has been implemented within the Blender framework in order to provide a highly configurable tool, able to reproduce different scenarios for Active Debris Removal missions.

The experiment has been performed over thirty parabolas offering around 22 s of zero-g conditions. Flexible meshed fabric structure (the net) ejected from a container and propelled by corner masses (the bullets) arranged around its circumference have been launched at different initial velocities and launching angles using a pneumatic-based dedicated mechanism (representing the chaser satellite) against a target mock-up (the target satellite). High-speed motion cameras were recording the experiment allowing 3D reconstruction of the net motion. The net knots have been coloured to allow the images post-process using colour segmentation, stereo matching and iterative closest point (ICP) for knots tracking.

The final objective of the activity was the validation of the net deployment and wrapping simulator using images recorded during the parabolic flight. The high-resolution images acquired have been post-processed to determine accurately the initial conditions and generate the reference data (position and velocity of all knots of the net along its deployment and wrapping of the target mock-up) for the simulator validation. The simulator has been properly configured according to the parabolic flight scenario, and executed in order to generate the validation data. Both datasets have been compared according to different metrics in order to perform the validation of the PATENDER simulator.

1. Introduction to active debris removal using thrown-nets

Proliferation of space debris implies expensive and risky operations in some of our most useful orbits such as LEO. More than 17,000 objects are tracked by the US Space Surveillance network, of which less than 1.000 are operational spacecraft. More than 66% is from over 200 on-orbit fragmentations that have been recorded since 1961. These are assumed to have generated about 700.000 objects larger than 1 cm. To date there are also 4 examples of collisions recorded. The space debris problem will be even worst in the near future as almost 1400 new satellites are expected to be launched in the next decade (Euroconsult forecast [1]).

Nowadays, all space agencies and space industry are realising a growing potential of on-orbit collisions (e.g. against dead satellites or used rocket upper stages) as the major source for new debris. Since the first awareness of the problem in the early 1960s, the global dimension of this problem has been understood today.

Studies at NASA and ESA [1], [2], [3] showed that the environment can be stabilized when approximately 10 objects per year are removed from LEO (with a removal sequence oriented towards the target mass). Active removal can be more efficient in terms of the number of collisions prevented / object removed, when objects removed have high mass, high collision probabilities and high altitudes.

ESA, with its Clean Space initiative focuses its efforts on four different branches: 1) Eco-design, 2) Green technologies, 3) Space debris mitigation and 4) Space debris remediation. ESA is investigating a range of capturing technologies in two categories; a) pushing technologies (capture with robotic arm), and b) pulling technologies (capture with nets or harpoons).

The use of throw-nets seems particularly promising for capturing objects in space in cases where robot grasping will be difficult (targets may have unpredictable spins and no suitable grasping points). Capture with throw-nets does not require complicated close-proximity guidance, navigation and control (GNC) loops, and consists of much simpler mechanisms than you would need for a robotic capture. The flip-side causes difficulties in the stabilisation of the stack post-capture. A similar activity (AdriNet [4], [5]) performed in parallel to PATENDER has been funded by ESA. Previous studies on flexible capture devices [9] were inspired by fishing technologies [11]. Last research studies regarding simulation of nets for ADR are related to the use of vortex dynamics [6], analysis of the critical deployment parameters [7] or IOD missions [8].

Testability and simulation are critical aspects to be addressed in order to mature the throw-nets technology. For this purpose ESA has funded several activities to develop simulators that can accurately represent the complex contact dynamics of a net wrapping around a tumbling body and, at the same time, they can be executed fast enough to perform statistical analysis. Additionally, these simulators were requested to be validated in an extensive campaign composed by a series of 0-g tests where throw-nets must get deployed and capture a target mock-up.

The net dynamics simulator has the aim of reproducing the behaviour and the effects of capturing space debris using different configurations in terms of net shape and dimensions. It can reproduce the net dynamics during the following phases: launching, deployment, target wrapping and deorbiting manoeuvres (refer to [10] for detailed explanation of deployment and contact dynamics). The PATENDER simulator has been validated by results gathered during a Novespace parabolic flight (Aircraft A-310, June 2015) where microgravity conditions can be reached during 22 s. The aim is to reconstruct the trajectory of net knots and corner masses (named as bullets along this paper) over time during deployment and mock-up wrapping in order to validate the numerical simulator. The parabolic flight experiment will also raise the technology readiness level (TRL) of space throw-net techniques to TRL 5/6 (representative prototype tested in a relevant environment).

This paper is organized as follows: Section 1 begins with an introduction to active debris removal (ADR) using thrown-nets, Section 2 explains the architecture of the thrown-nets simulator, Section 3 describes the designed experiment for microgravity conditions, Section 4 shows the 3D

reconstruction results, Section 5 describes the validation of the PATENDER simulator and Section 6 presents the conclusions.

2. Architecture of the ADR Thrown-nets simulator

The thrown-net simulator framework developed within the PATENDER activity (see Fig. 1) is able to perform simulations of large particle systems with advanced 3D visualization capabilities. This capability requires a visualization tool that takes advantage of the Graphics Processing Unit (GPU). The identified development environment for the simulator is Blender,[1] which provides a comfortable and open-source framework able to be parametrised trough Python[2] scripts. Such scripts provide a parametric and automatic execution of the simulations allowing to perform either manual simulations commanded by the user or Monte Carlo campaigns for statistical purposes. For the 3D visualization capabilities, the Blender/OpenGL[3] rendering engine motor is used.
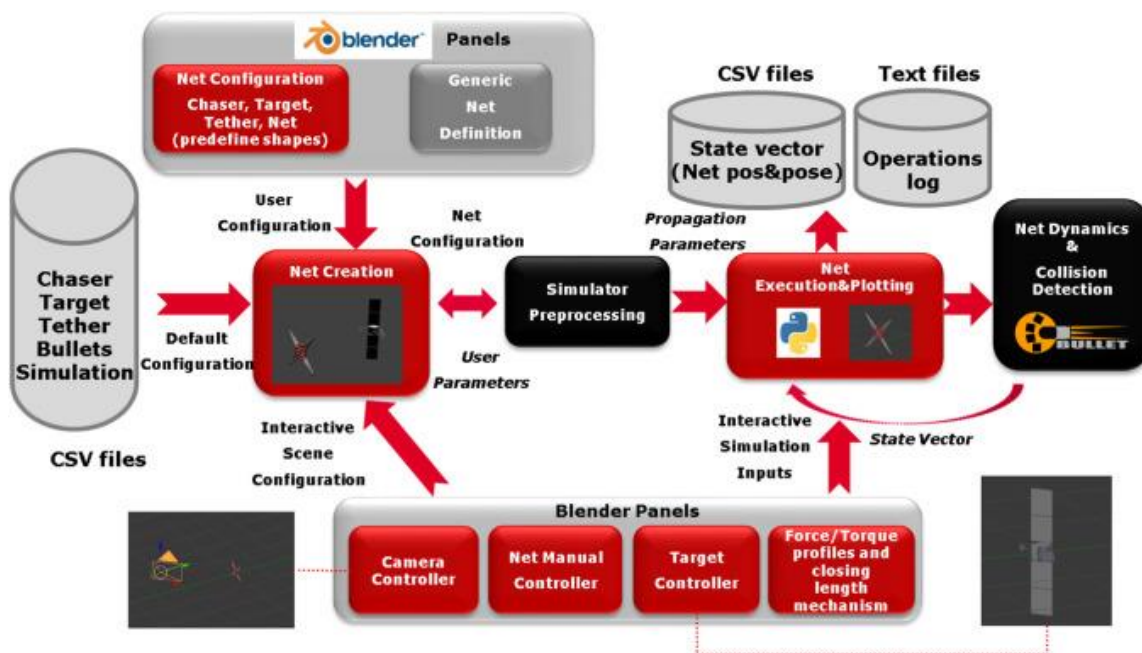

Fig. 1. PATENDER simulator architecture and data flow.

Within the PATENDER simulator, the user can create, move and visualise the net evolution considering different net configurations and environment settings. This simulator is divided into three main elements:

- Graphical User Interface (GUI): It is based on Blender and allows the user to interact with the net configuration, environment and execution.
- Simulation Environment: Python scripts necessary for the configuration, execution of the simulator and exchange of data with the Net Models.
- Net Models: External application (developed using C++ language) containing the autocoded Matlab/Simulink dynamics propagator, the collision detection functions (based in the Bullet[4] physics engine) and the contact dynamics algorithms (Hippmann, 2003 [12]).

The visualization of the net deployment has been implemented using Blender as a graphic interface and Python as a script environment. Several visualization capabilities have been developed in Blender in order to ease the communication with the Patender simulator. Therefore, through the GUI the user can perform the following operations: a) 3D visualization of the net deployment and

of the target capture operation, b) define the 3D view angle during the simulation, c) plot relative distance and relative speed measurements between any two net knots during the simulation, d) plot full state vector of any net knot or body (target or chaser) during the simulation, e) save the simulation visualization as video format and rendered images and, f) export the data obtained during the simulation to comma-separated values (CSV) and Matlab standard formats.

The net configuration parameters (net type: planar, pyramidal, conical or user defined; net size; number of strings and rings, etc.) together with the propagation parameters (a set of configuration parameters for fast computing of the propagation algorithms) are loaded from dedicated csv file into the simulator. The dynamic propagator performs afterwards, the step-by-step simulation of the net deployment and wrapping and it communicates the computed state vectors at each time-step through the communication channels to the simulator.

The net elements are created in Blender (for visualization purposes) as Blender 3D elements. Therefore, the net knots and bullets are represented by spheres of different dimensions and the links as cylinders. Links are defined as any thread between two knots and are subdivided into intermediate nodes and elements (see Fig. 2) for a better representation of the net impact on the simulation target. The tether, which connects the chaser with the net, is also modelled as a link, discretised into nodes and elements. Moreover, the user can choose at the beginning of the simulation the inclusion of an additional link (closing link) to ensure the capture of the target after initial wrapping.
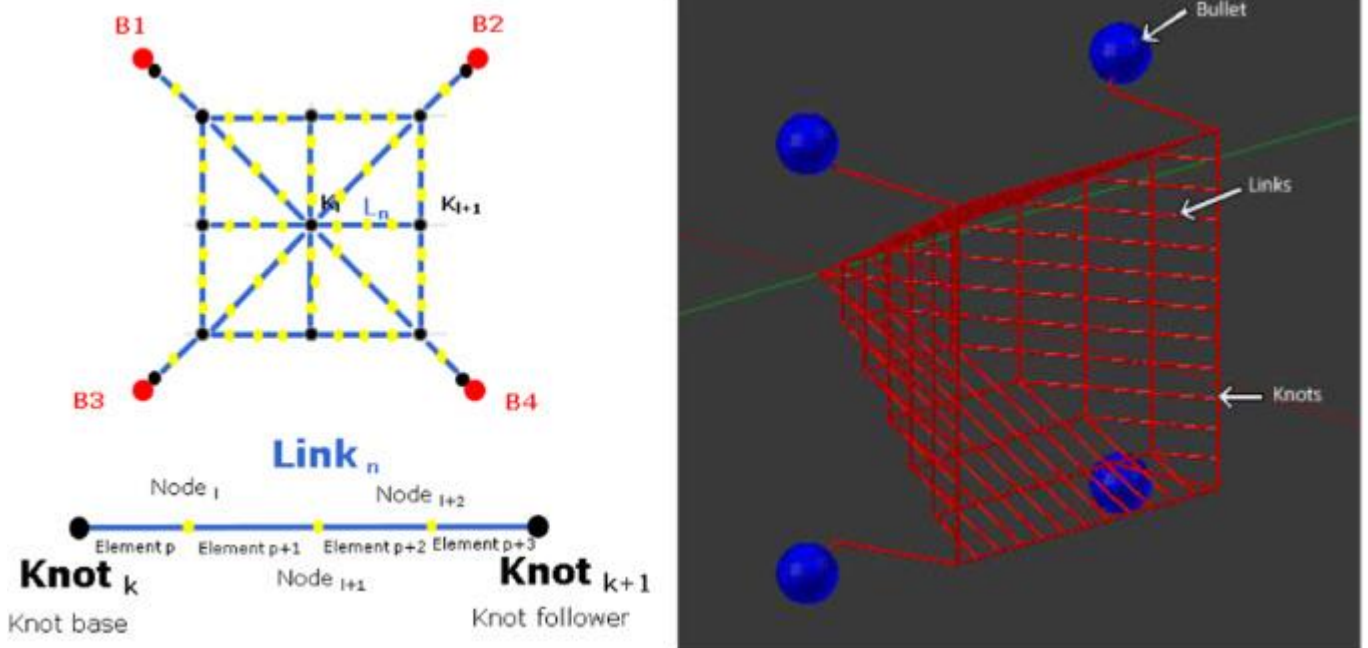

Fig. 2. Net elements (knots, links, bullets and nodes) definition (left) and Blender representation (right).

The Python scripts are composed of python classes that hold all configuration elements of a net scenario and related capabilities to update the position of the net elements within the 3D Blender environment.

The initial position of the net corresponds to the vertex at the top of the canister and the corners at the top, according to canister size. By defining the canister size the distribution of the knots is computed automatically distributing them along the canister from top to bottom. The bullets can be either attached to the corners of the net or attached to the net through bullet links. The closing links are attached to corners (either knots or bullet if no bullet links are present); they can be either present or not, if they are present two configurations are possible: four links attached to the four corners or n links attached to all knots of perimeter.

The initial velocity of all the net knots, nodes and bullets is given with respect to the chaser conditions; the shot velocity is added only to bullets by just specifying the modulus of the initial launching velocity relative to the chaser and the divergence angle relative to the Net reference frame (local body frame placed at the chaser Centre of Masses (CoM) where the X axis is parallel to the axis chaser-target CoM's and points forwards towards the target, the Y axis is transversal to the axis chaser-target and points towards the left and the Z axis is vertical to the axis chaser-target and points up with respect to the observer).

When the execution is started, the state vector is updated through periodical calls, changing the net location accordingly. Each net element receives from the autocoded net model through the state vector the updated position (on the XYZ axes). Once the net is created, the simulator provides several capabilities that can be applied to the net, such as:

- Plot the net trajectory by marking with a sphere the last position of the net in each simulation step;
- Point, through arrows located at the bullet centre, the net deployment direction;
- Plot the relative distance between two knots;
- Enable image rendering to be used either for net images display or for video creation;
- Plot the elements state vector by selecting the element type (knot, node, tether node; bullet, chaser or target) and index for position, velocity, acceleration and forces value;
- Save the net components state vector into csv files;
- Delete the net;
- Reset the net by moving the net to the initial position by deleting first all elements from the scene and then re-creating the net at the initial position;
- Regenerate the net at the previous saved states.

The chaser and the target are imported as a CAD file at the initial position set by the user through the initial state vector. Moreover, the target can also be subject to actions such as scaling, change on the position, saving of the states and relocation the target at the saved position. Fig. 3 below shows the rendered image of a net (13×13 knots) deployment and wrapping around a target representing a satellite that is imported from a CAD file.
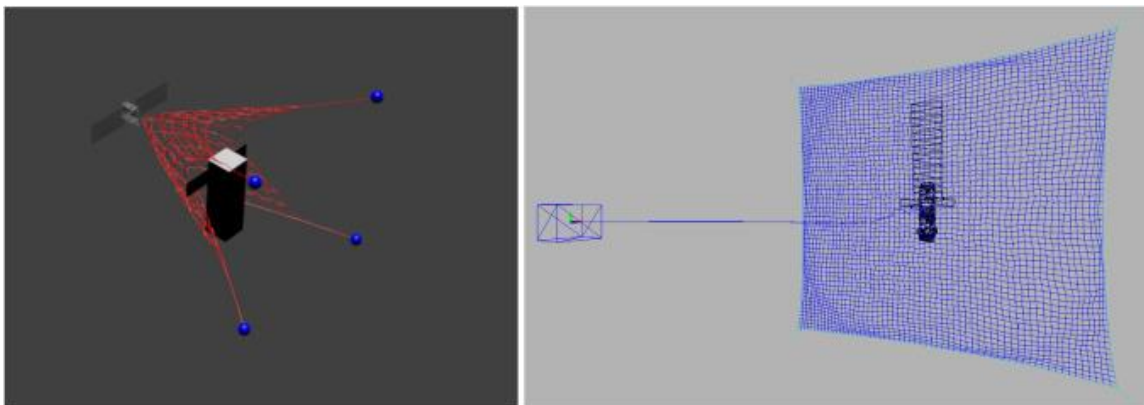

Fig. 3. Example of partial net deployment (left) and full deployment (right).

The Patender simulator has also the capability of running Monte Carlo simulations. This is carried out for a certain period (selected by the user) and avoids plotting in the Blender scene the evolution of the net, in order to speed up the simulation processing time. It has the advantage that given the setting of the simulation time, the user can run this function and save the state vector for different user parameters.

The creation and the CPU execution time are directly proportional to the number of degrees-of-freedom (DoF) of the configured net. The DOF is computed as a sum of the number of knots, bullet number, total number of nodes, total number of nodes on the tether and additional ten DOF's for each bullet and rigid body (chaser and the target). In Table 1 below it can be found an example of how the Net creation time in Blender increases with the net size.

3. Design of the thrown-net experiment under microgravity conditions

3.1. Parabolic flight profile

The PATENDER experiment was flown on the Novespace 116th parabolic flight campaign (62nd ESA Parabolic Flight campaign, June 9th, 2015) on board of an Airbus A310 aircraft. A typical Novespace parabolic flight is composed of 31 parabolas in a roller-coaster mode where six series of 5 parabolas are concatenated with short breaks of 1 min and 45 s between them. Each parabola has a duration of ~22 s with a microgravity maximum level of 0.05 G and it is preceded and terminated by acceleration periods of 1.8G during 2–3 s as shown in Fig. 4 below. After each set of parabolas a long break of 5–8 min allow to perform minor adjustments of the on-board experiments.

Net size (Horizontal and vertical knots)	7×7	13×13	19×19	25×25
Net DoF	777	2505	5313	9201
Net Creation time (sec)	3	11.6	80	480

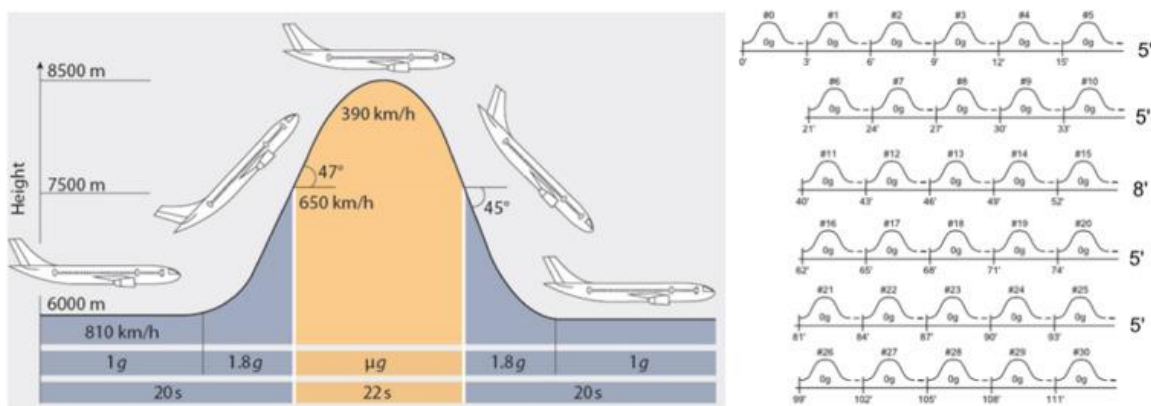Table 1. Net Creation time vs net size and DoF.

Fig. 4. Novespace parabola profile (left) and VP116 flight profile (right).

3.2. Experiment safety data package

Parabolic flights do not represent a public air transportation activity and it does not follow typical certification processes of Airworthiness (CoA). Instead of that Novespace manages the flight according to internal security procedures. The PATENDER experiment has followed a strict certification process to determine and accommodate safety rules established by Novespace. An Experiment Safety Data Package has been elaborated together with Novespace enabling the execution of the PATENDER experiment (see Fig. 5) on-board the Novespace aircraft.
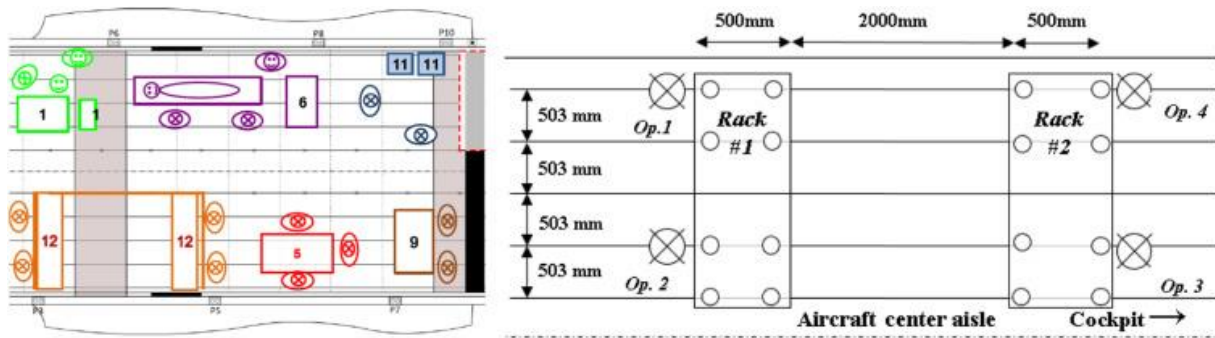
Fig. 5. PATENDER experiment distribution: Number 12 within A310 aircraft (left) and racks/operators (right).

The design, fabrication and assembly of the structures, as well as attachment of the equipment onto the structures, were carried out under the supervision of Novespace mechanical experts. Maximum allowable loads have been defined to make sure that the structure will sustain an emergency landing. Rigorous procedures for ground and in-flight operations (as shown in Table 2) were identified allowing to determine the required number of operators and to identify the role executed by each one.

Task	Description	Operator
1	Calibration of cameras set-up using a double chessboard	1
2	Adjustment of bullet liners angle	2
3	Review of cameras and recorders	3
4	Adjustment of launching pressure	4

Table 2. Example of in-flight procedure.

Finally the PATENDER experiment was evaluated from the point of view of hazardous risks grouped into the following categories: fire, electrical shock, structural failure, contamination, collision, injury/illness, explosion/implosion and any other. The following major hazardous risks have been identified and appropriate hazard controls and verification methods have been proposed:

- Contact of operators with voltages above 32 V (defective wires, insulation or short circuits).
- Experimenter gets hit or injured by the net/masses (staying of operators in the cage during the launch, premature triggering of the launch or excessive initial velocity of bullets).

3.3. Set-up of launching system and racks

During the experiment under micro-gravity conditions, the net launching system carried out the net reload, pneumatic recharge and launching operations. The structure of the net launching system is based on a metallic table composed of two parts. The first one is a support table to accommodate all other elements. The second one is a turning plate whose purpose is enabling angular placement of the motherboard to ease the direction of the net launching throughout experiment. This turning plate includes two hinges, a key and a cog and it allows 180° rotations (by increments of 15°). Over such turning plate, it is placed a motherboard where the rest of the elements are integrated. These elements are: four bullets, four bullets liners, four angle-adjusting mechanisms and a net container support (see Fig. 6). Besides, it includes a structure made of aluminium profiles and metallic joints holding the storage tank, the support table and an electrical connections box.

Fig. 6. Motherboard with integrated elements (left) and different type of manufactured bullets (right).

The mechanism to adjust the launching angle of the bullets (see Fig. 7-a) can be operated independently for each bullet. It allows adjusting an angle range from 15° to 45°, measured from the vertical line/axis. Bullet liners are the mechanical guidelines where bullets are placed (including O-rings to adjust friction required force). Through these liners, the pressurized air flows out inducing the ejection of the bullets and consequently of the attached net. Bullets design criteria are geometry, mass and centre of gravity. These design criteria allow bullets to be pushed away over the bullet liner by means of pressurized air. The contact point between the air flow and the bullet must be located under its centre of gravity in order to ensure a longitudinal motion. The pressurized air flow is activated by the electrical/pneumatic system.

Fig. 7. a) Adjustment mechanism of bullet angles (left) and b) Operating handling the net reload tool (right).

Due to the timing constraints imposed by the parabolic flight characteristics, the net container was designed as an independent element from net launching system. As a result, a reload or charge/discharge tool has been designed to ease operator tasks and optimize the time between parabolas. This reload tool (see Fig. 7-b) allows an easy assembly of bullets and net into the canister.

The canister or net packing container is the element where the folded net is placed. Additionally, this canister is placed inside its support by an adjustment system. The canister is placed in the support and its position is fixed thanks to lateral jugs and magnets. This approach allows placing several types of containers depending on geometry requirements of the net. The net launching system includes a cover over the canister and its corresponding opening system. The cover is integrated in the container support and it is articulated without interfering with the ejection of the bullets. This articulation is made of a set of antifriction bearing bushes to permit an easier turning. The cover is opened due to the force of two torsion springs. This force is constant until the locking system of the cover is opened. The cover opening is triggered by a dedicated delayed relay of the electrical system. This set of elements are the mechanical parts which will enable the launch process.

The pneumatic system permits pressurized air to launch the bullets at desired initial velocity and angle. It is controlled by an electrical system (see Fig. 8) composed by several relays and activated externally by a remote control in the hands of the operator. The feeding air flow is pressurized air

passing at 6 bar through a filter and a manometer. After going through the manometer, the air flow is under the pressure range manually selected by the operator (within 1 and 4 bar). Then, the air flow is directed to the V5 valve to fill the air tank as shown in Fig. 8. Afterwards, when the bullets launching is carried out, the pressurized air flow goes through valve V4 and it is divided into four lines to reach the four bullets. After activation of V4 valve, the bullets are pulled by means of the pressurized air through bullets liners.
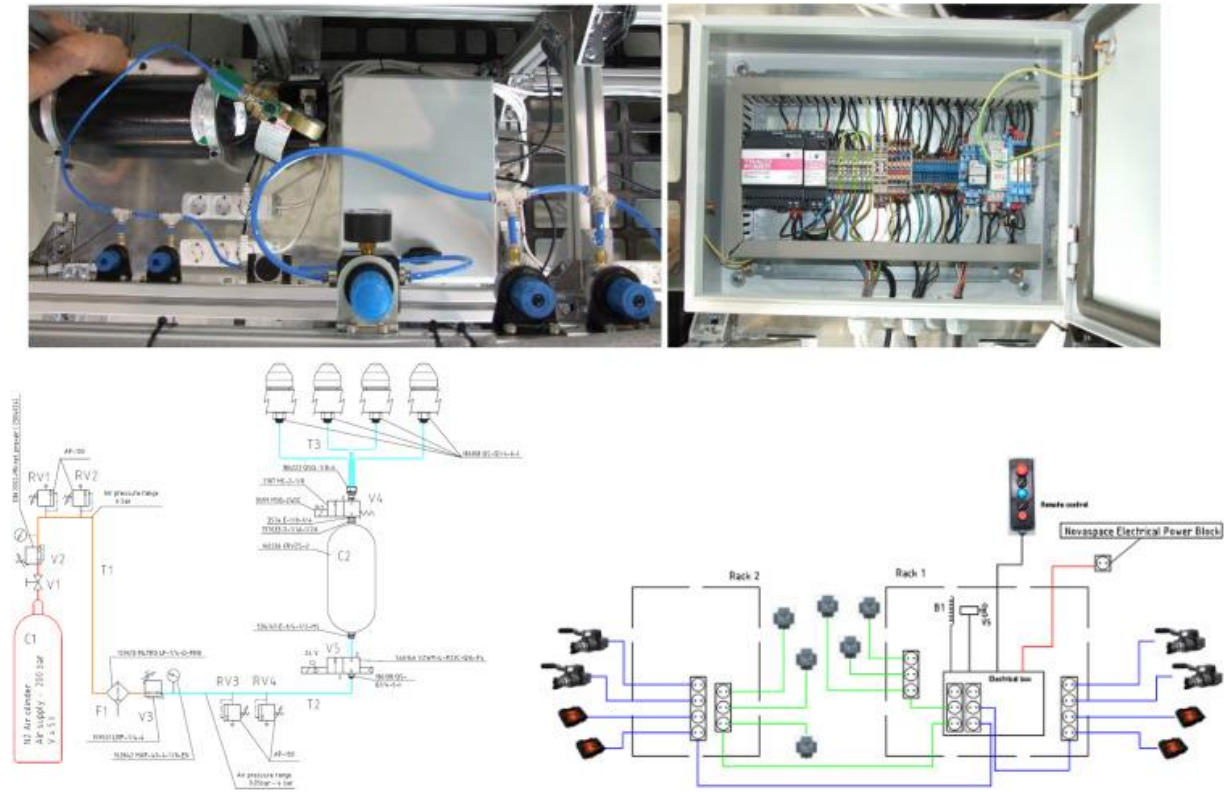

Fig. 8. Pneumatic elements (left) and electrical diagram (right).

The overall process to carry out the net launching is as follows: first, the operator must activate the system through remote control. Once it is activated, the operator presses the launch button and the pneumatic system proceeds as detailed above. At this time the cover of the canister is opened and, after a delay time of 1 s (configured in a relay), the compressed air contained within the cylinder C2 is released through the valve V4. This compressed air is conducted to each bullet liner through tubes of equal length. The bullets are pushed by the air pressure until they leave completely the bullet liner and they start flying without any other restriction. Once the launch is completed, the operator turns off the launch activation system via the remote control. In consequence, the valve V4 is closed and V5 is opened. Then, the air cylinder is recharged with air from the air feed system. After the net and the bullets are replaced in the launching system and the cover is closed, the complete equipment is ready to execute a new launch. Fig. 8 below (left) shows the pneumatic scheme of the net launching system while Fig. 8 (right) shows its corresponding electrical diagram. The PATENDER experiment has required a specific set-up adapted to the parabolic flight requirements by means of two independent racks whose elements were placed as shown in Fig. 9 below: rack #1 on the left and rack #2 on the right. The rack #1 is composed of a metallic structure where the required elements are placed: two cameras, lamp plates and the net launching system including separately an air tank, an electronic box and the pneumatic system. The two cameras are placed on the top corners of the structure; at the centre it is placed the net launching system. At its back it is positioned the air tank (5l N2 air cylinder at 200 bar). The electronic box and the pneumatic system are situated at the bottom of the rack and connected to the rest of components.

Finally two light-emitting diode (LED) lamps (12VDC, 100 W) are placed at the bottom of the structure and the whole rack is fixed to the floor using four screwed plates.
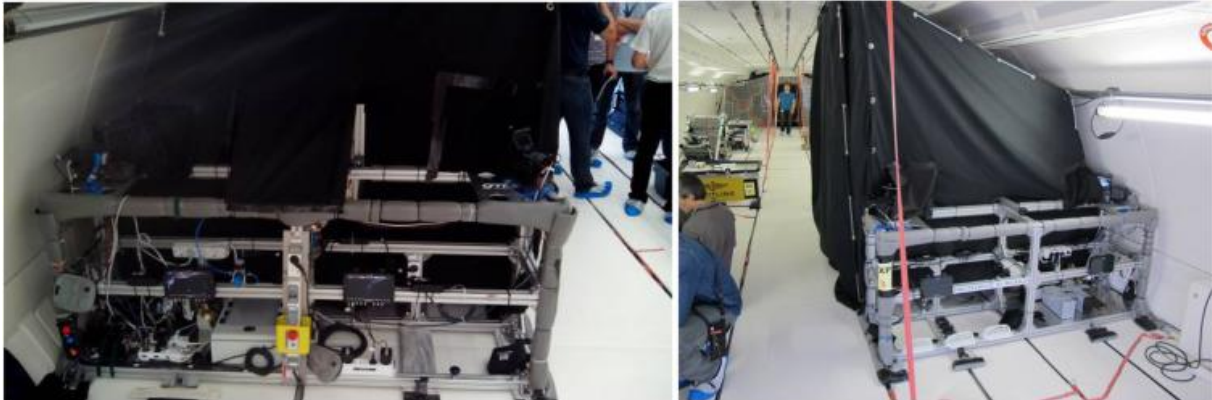

Fig. 9. Rack #1 holding the net launching system (left) and rack #2 holding the satellite mock-up (right).

The rack #2 holds other elements such as the satellite mock-up and two other cameras. At the bottom of the rack structure two LED lamps are placed (i.e. a total of four LED lamps) to illuminate the overall scenario while the experiment is recorded. On the top of the structure, the two cameras are placed at a distance between them of 2 m. In the middle of them, a structural arm supports the mock-up. This arm can be extended up to 300 mm and it can be turned within an angle range of ±90°.

3.4. PATENDER experiment design: Net and Target mock-up

The PATENDER experiment within the parabolic flight was prepared with up to six nets (6) made of Technora, an aramid fibre well known for its high strength (Young Modulus of 7.3e10 Pa, density of 1390 kg/m^3 and threads diameter of 1 mm) and approximate dimensions of 0.6×0.6 m and 50 g of mass. The net has a squared shape (folded net takes up 10×10×10 cm) and each of its corners is attached to a massive bullet (200 g, 5×5×5 cm); its total mass is ~850 g. The net is being hold in a container and deployed pneumatically by a launching system. After a horizontal motion of approximately 2 m the net is fully deployed and wraps the satellite mock-up. The satellite mock-up is made of a rectangular block whose dimensions are 0.075×0.125×0.250 m with an antenna array plate of 0.25×0.05 m. Both the net and the target mock-up are representing a simplified capturing exercise of the Envisat satellite. This capture has been reproduced at a geometric scale of 1:40. Several simulations were performed to analyse the maximum expected relative deviation due to the aircraft pitch angular velocity within the parabolic flight. We were concluding (see Fig. 10) than as long as the shooting direction was coincident with the roll axis: a) the vertical deviation was always positive (minimum of 0.9 m and maximum of 2.2 m); b) the longitudinal deviation was positive as long as the shooting point is at a positive distance from the CoM at least equal to the cabin length and c) there is no lateral deviation, whichever the shooting velocity and direction orientation. This analysis was partially confirmed during the parabolic flight (as the residual and random microgravity conditions of 0.05g were requiring a higher initial velocity to avoid such perturbations).
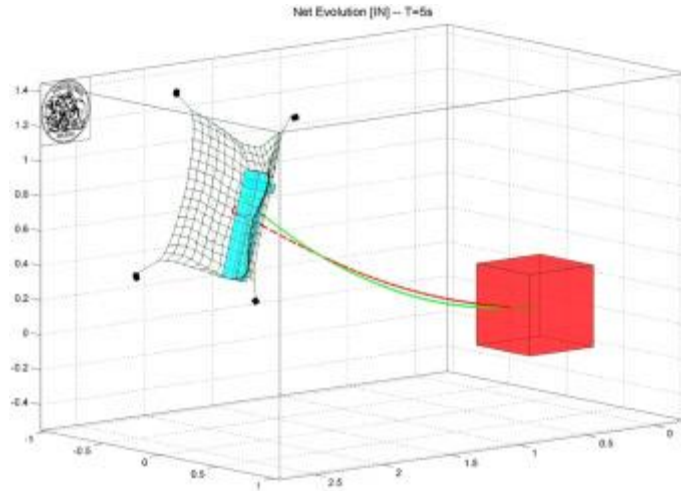
Fig. 10. Net deployment simulation results including the aircraft pitch angular velocity.

3.5. 3D Reconstruction set-up

Four Sony Nex-FS700RH cameras were recording all net launches at 60 fps in 4 K resolution in order to allow the 3D reconstruction of the deployment and wrapping around the target. Such high needed resolution is due to the requirement on the ratio between net knots size on pixel size, which must be above 5/6, to guarantee knots extraction robustness. An increased shutter speed has been selected to minimize the motion blurring effects while preserving a sufficient luminosity of the image.

The cameras have been placed as far as possible from each other to increase both the baseline (reconstruction accuracy) and the area that their field of view can cover with an acceptable resolution for reconstruction. They were placed in landscape configuration on top of the racks for stability purposes (e.g. to minimize their vibrations) and rotated around Z-axis of 45° and 35° for the front stereo-couple and the rear pair respectively. The focal length was set to 14 to reach the needed field of view; however such a wide angle requires finer calibration, especially at boundaries, to minimize distortions. The gain was set to 6, after saturation analysis; the iris aperture and focus were finally tuned to allow the correct depth of field. The shutter speed has been tuned to 1/1000 s to limit blur as much as possible due to net motion, while keeping a sufficient amount of light.

Fig. 11 below shows the field of views and stereo couple coverage for both the front and rear pairs. Setting up a synthetic environment as the one presented in Fig. 11 and Fig. 12 has been proven to be very useful allowing a finer tuning of the camera settings in the experimental set-up.
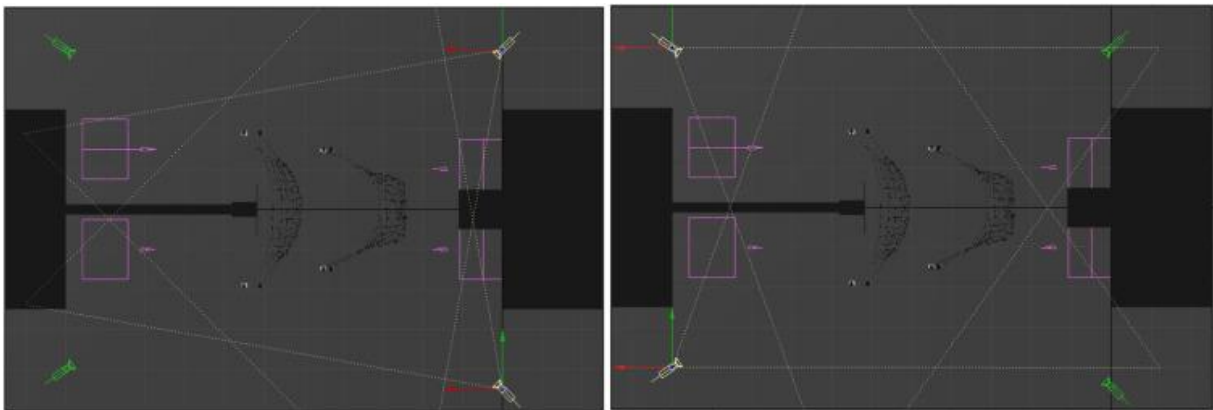

Fig. 11. Fields of view and stereo coverage – front and rear stereo pair of cameras.
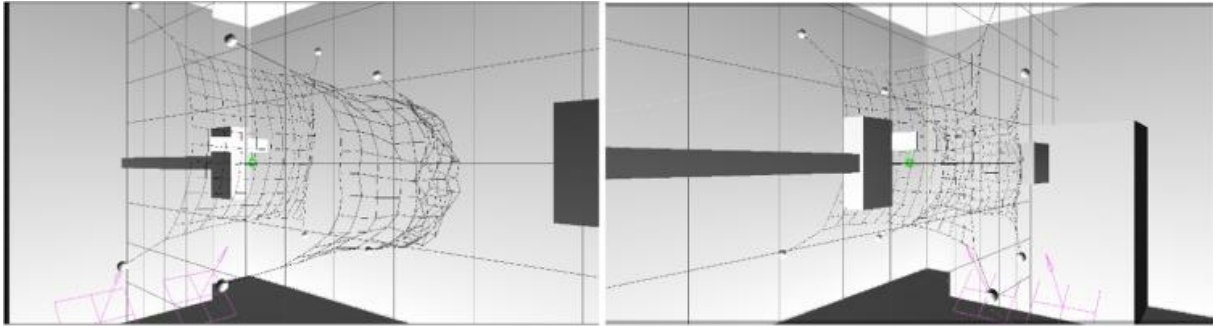
Fig. 12. Net simulated deployment – front and rear views.

Net knots were colour-coded with fluorescent pigments using a 4-colour coding system (yellow, red, cyan and green) as reconstruction algorithms are based on colour-segmentation (as one of the simplest and robust methods to track elements at high speed). A uniform background was necessary as well as proper illumination: a LED-based illumination system was placed on the floor and was selected to meet parabolic flight safety constraints (heat, luminosity, operations and failures) and lighting conditions requirements, being very demanding with the needed resolution, frame rate and shutter speed.

Finally, two independent inertial measurement units (IMU) were synchronized with the system during microgravity tests to record acceleration profiles, as another key feature for the posterior model validation. The primary IMU was calibrated with the cameras position (having the secondary IMU as backup) in order to give as an output the accelerations and angular rate profiles in the master camera reference frame, being the reference frame for 3D reconstruction.

Fig. 13 below shows the configuration and integration of the set-up (area of 3×2 m) on board the Zero-G A310 while Fig. 14 shows two screen shots of the wrapping and capture of a mock-up representing the Envisat satellite.
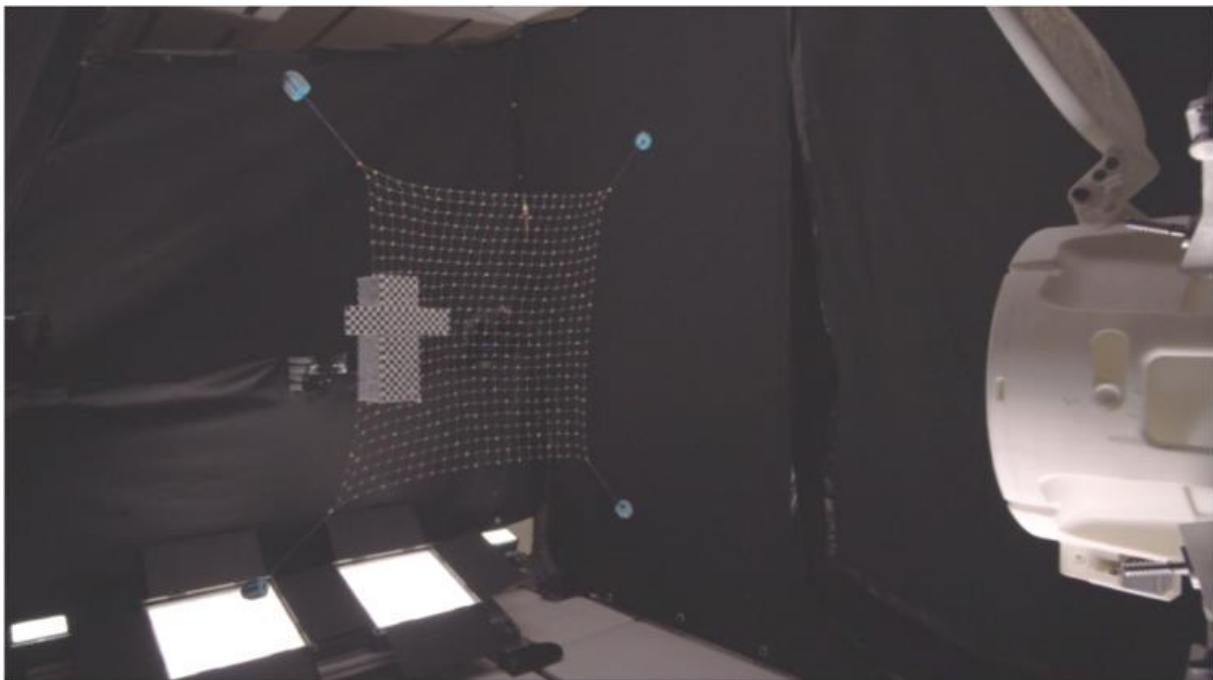

Fig. 13. Flight configuration and experiment integration on board Zero-G aircraft.
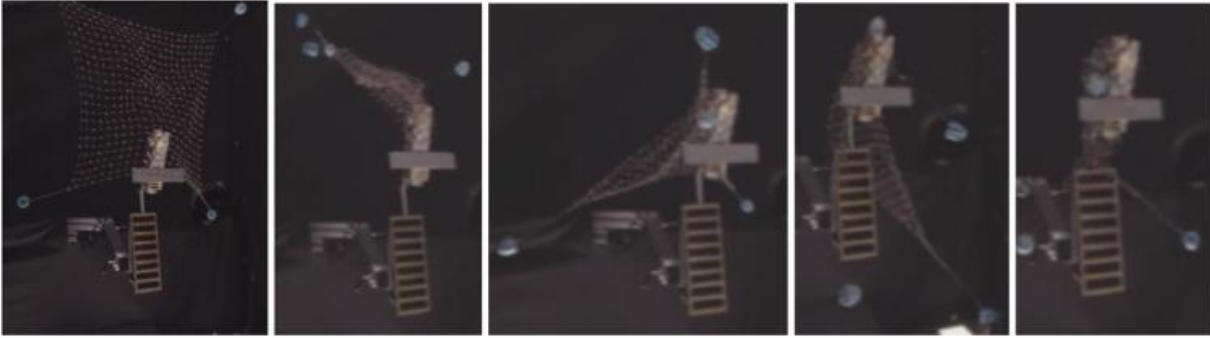
Fig. 14. Sequence of wrapping and capture of the Envisat satellite mock-up.

4. 3D reconstruction process and results

The PATENDER experiment was successfully flown on the ESA-Novespace parabolic flight of June 9th, 2015; the launch of the net was performed during all the thirty foreseen parabolas. We experienced a total of 7 failed launches due to non-simultaneous ejection of the four bullets. By reducing the number of friction rings on the bullet liners and increasing the initial velocity of the bullets we were able to increase the launching success rate up to a total of 23 parabolas (including 3 launches using a realistic Envisat mock-up). After the post-processing of the usable 20 parabolas, a total of 9 parabolas were selected for 3D reconstruction (5 parabolas were non-reconstructable and other 6 were having a reduced quality due to a very high launching speed not allowing to perform the 3D automatic reconstruction process). A deployment and wrapping sequence is reported in Fig. 15 below, as an example of successful capture, as visible from one of the front cameras.
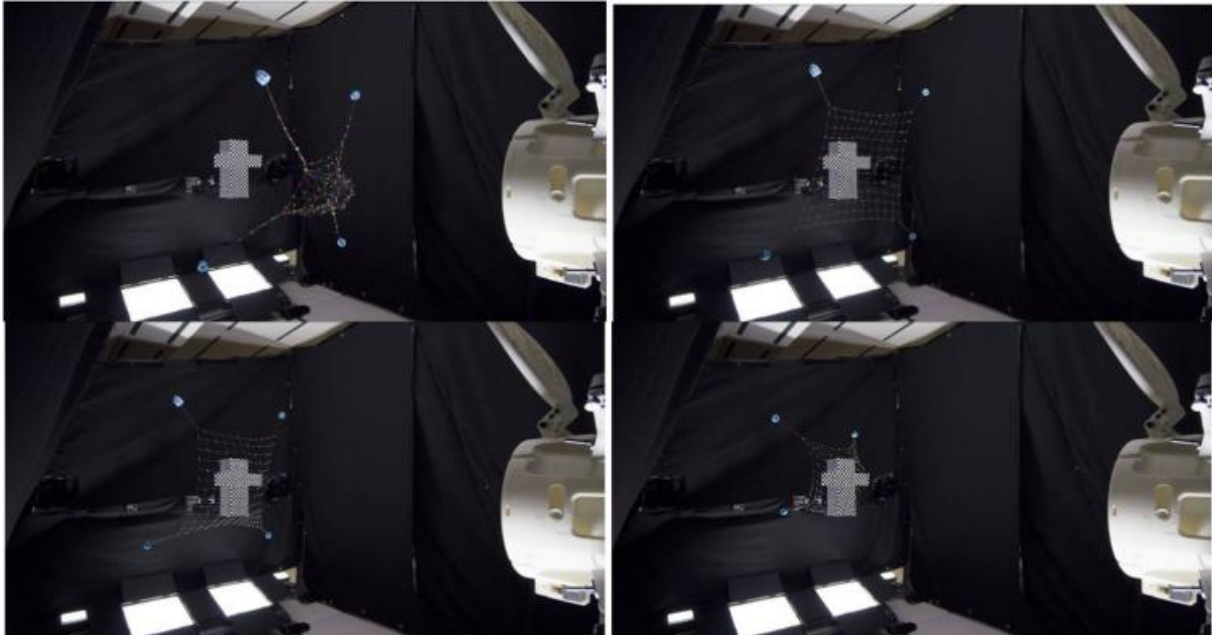

Fig. 15. Microgravity experimental capture sequence of four screen shots (from left to right).

The four cameras synchronization was performed through a microcontroller board (Arduino-based), using the Sony logic application control bus system (LANC) protocol. The board accepted as input a transistor-transistor logic (TTL) signal for start and stop to connect the cameras system to the rest of set-up (IMU, lights and shooting system). The microcontroller was feeding to the cameras a white noise audio signal, the correlation of which allowed to synchronize the four videos a posteriori.

The intrinsic parameters of each camera were calibrated through the use of a standard calibration procedure using a checkerboard. Also the stereo calibration was performed in a similar way: using a double faced checker board, it is possible to calibrate the entire set-up at the same time by calibrating cameras two by two. The size of the checkerboard was defined according to the envelope covered by the cameras derived from their field of views, in order to be visible by the four cameras at the same time. The calibration was performed after take-off and before landing, to be able to partially correct possible cameras displacement during the parabolic flight.

The 3D reconstructions procedure is based on the image processing for colour segmentation (to this end, net knots have been colour-coded with fluorescent pigments as previously mentioned), stereo matching of the segmented knot and iterative closest point (ICP) for time tracking of knots, as described in [13], [14]. The algorithms developed at Politecnico di Milano have been adapted for the specific features of this experiment and successfully tested on ground before the flight. An example of colour segmentation and knots localization is presented in Fig. 16 the first image is the result of raw file processing for white balance and gain correction, the second one is the yellow filter and the third one is the final binary image exploited by the reconstruction algorithm.

Fig. 16. Colour segmentation of yellow knots: processed image from raw, yellow filtering and final binary image.

The knots topology is reconstructed when the net is completely deployed, and a univocal identifier is attributed to every knot. The main step of the 3D reconstruction procedure is based on knots matching along the epipolar lines: during this step, even for the completely deployed net, two problems were found:

1. The first one is that since the net lattice can be thought in terms of a transparent surface and all the knots are similar one to each other many ambiguous matching along the epipolar line will occur.
2. The second problem is that in some cases, the net itself hides some knots in a view and thus, it is impossible to find the corresponding knot on both views.

Taking just the closest point to the epipolar line can generate reconstruction errors since the higher closeness to the epipolar line with respect to other knots could be due to low resolution, not perfect barycentre extraction from blobs after the segmentation step and not exact lens distortion compensation in peripheral image regions. In order to minimize these problems the average plane of the 3D reconstructed points is defined at initial frame, being the net planar when completely deployed: its normal direction is the singular vector associated to the lower singular value of the SVD from the 3D points (it represents the direction of lower variation of the 3D point cloud).

As a second step, the plane estimation is refined taking only 3D points whose distance from the plane falls within the first three quartiles of all distances. The 3D position of every knot is then refined introducing a penalty on the matching epipolar line based on a weighted sum of the distance from the epipolar line, the distance from the average plane and the distance from the neighbour points (the maximum knots distance, based on an elongated thread length, is used as a last consistency check to stop the iterative repetition of the previous). Then the tracking step is performed backwards and forwards for every knot until they become occluded from both the stereo pairs. The tracking step further reduces these errors by using as constraint that, between two consecutive frames, every knot should occupy the closest allowed position to a knot in the previous frame and that the maximum distance between knots cannot be greater than the mesh size.

As a first step, it is extremely important to minimize the overall calibration error: this affects in fact the precision achievable by the following triangulation and stereo reconstruction procedure. An example of successful calibration results is given in Fig. 17 for one pair of cameras. Out of more than 16.000 calibration images, 65 good couples were selected leading to a residual error of 2 pixels: this error has proven to be too high to obtain fine results in the triangulation. By selecting the top 28 couples among the best, it is possible to further minimize the calibration error. In particular, with this calibration, the mean residual error results to be 0.53 pixel as shown in Fig. 17. It is extremely important to keep the overall calibration error under one pixel: this affects the precision achievable by the following triangulation and stereo reconstruction procedure.
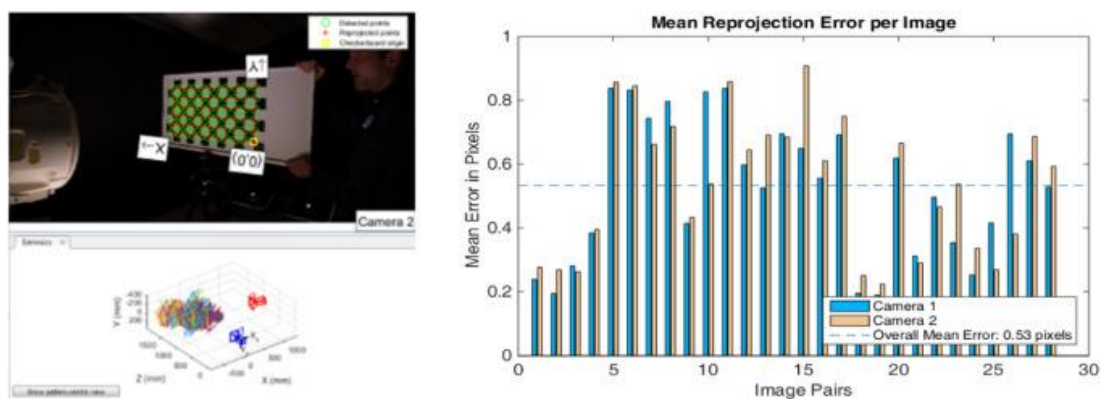

Fig. 17. Calibration results (left) and mean reprojection error (right).

Good colour segmentation results were obtained using Hue segmentation in the Hue-Saturation-Value (HSV) colour space: 96% of the visible knots were correctly identified. Some spurious colours, due for example to reflections, are possible but eliminated either manually or during the tracking step.

The target mock-up position and orientation in space is reconstructed by the checkerboard applied on it, the face plane is identified in space and then its position vector and orientation matrix are derived from geometrical constraints and easily inserted in the simulator as input parameters. Fig. 18 shows the reconstructed mock-up face and antenna planes. Its position vector and orientation matrix are derived from geometrical constraints and inserted into the simulator as input parameters.
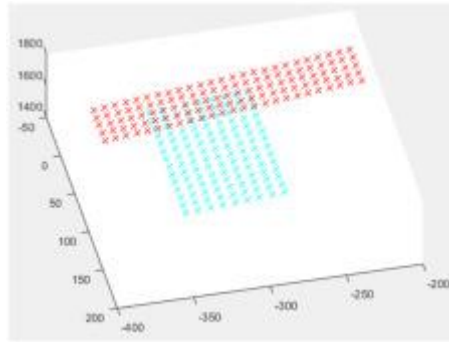
Fig. 18. Reconstruction of target mock-up.

Fig. 19 below presents the reconstruction of the net topology between two subsequent frames. All the points are correctly segmented by their colour and the stereo matching is accurate. From the comparison with the real images, a good correspondence can be observed.
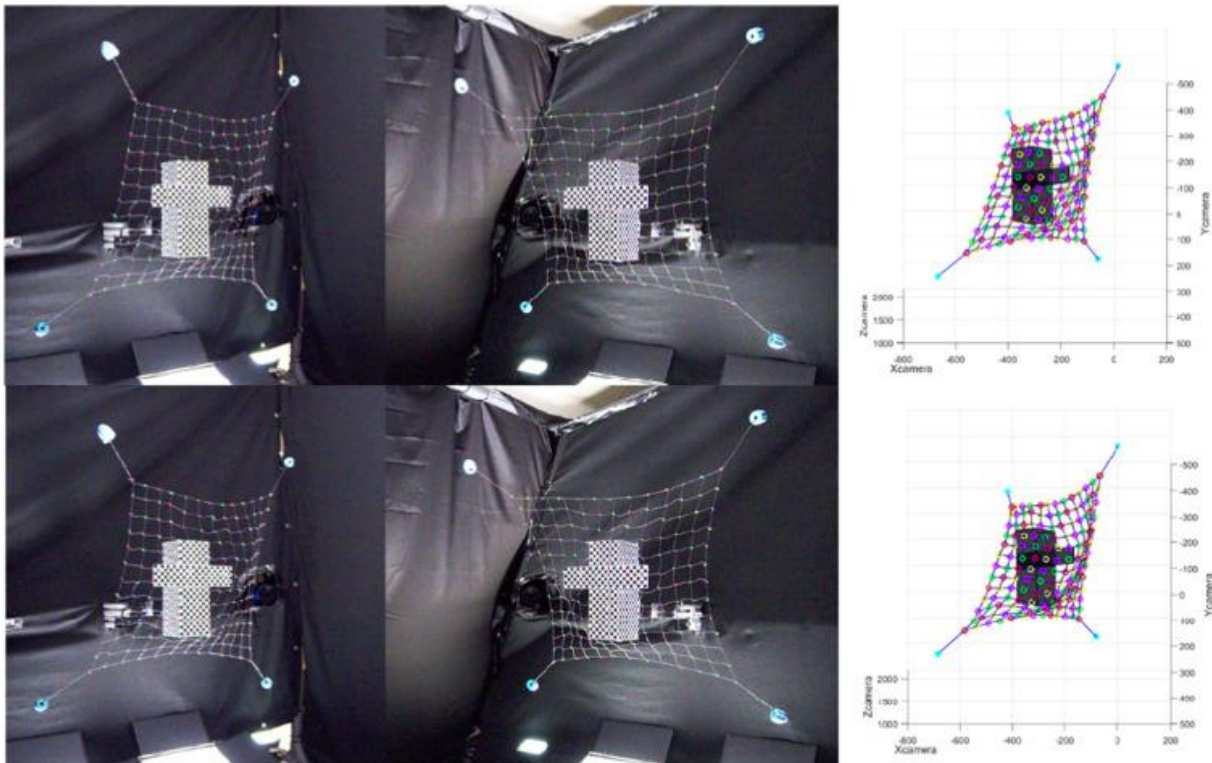

Fig. 19. 3D reconstruction of two subsequent frames.

The overall accuracy of the 3D reconstruction process can be determined by evaluating the minimum distance in space between the two epipolar lines corresponding to the same point in the left and right camera frames respectively. This value is used as an index to describe the 3D reconstruction error. The individual 3D reconstruction error of each knot in a single frame (frame N = 282 of parabola 17) is represented by Fig. 20 below where the net is completely deployed. This figure also shows the mean 3D reconstruction error over 160 frames demonstrating that the referred maximum error is always lower than 5–6 mm. In particular, good results are achieved in the first part of the parabola (error below 2 mm) when the net is completely deployed and the knots matching is easier. During the first part of the wrapping phase between frames 20 and 80 the error is increased up to 4–5 mm. This phase produces higher errors due to the complexity of associating univocally each knot with the corresponding ones in all the cameras In the final part of the

wrapping after frame 80, the mean error is reduced down to 1–2 mm due to the lower number of detected knots.
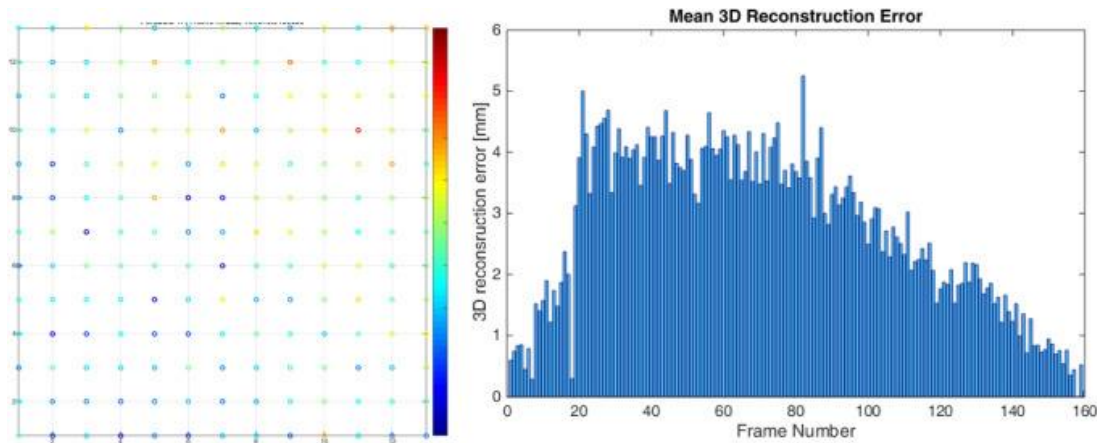

Fig. 20. Parabola #17: 3D reconstruction error in scale 0–5 mm (left) and mean 3D reconstruction error in mm over 160 frames (including deployment and wrapping phases).

The 3D reconstruction process of all the foreseen nine parabolas has been a laborious process performed between June 2015 and September 2016. In particular, in two of them (parabolas #27 and #30), the net is composed by a 24×24 knots mesh with a square shape of size 0.9×0.9 m and in the remaining other seven parabolas (#10, #11, #16, #17, #18, #20 and #26) the mesh is 13×13 knots with a square shape size of 0.6×0.6 m. For each parabola, they have been analysed and reconstructed 200 frames per camera (a total of 7200 images). The knots have been identified through the described semi-automatic algorithm and the bullets were manually identified for each frame.

As partial result of the global 3D reconstruction process, three images representing three different instants of the parabola (the first, the last and an intermediate frame) are shown in Fig. 21 below. From these figures, it is possible to confirm the proper 3D reconstruction of the net knots in all the parabolas presented. Moreover, the reconstruction is not dependent on the initial conditions and shape of the net. In the final part of the wrapping phase, only the visible points on the target are correctly tracked and reconstructed. The target is accurately reconstructed in each parabola, independently from its position and orientation.
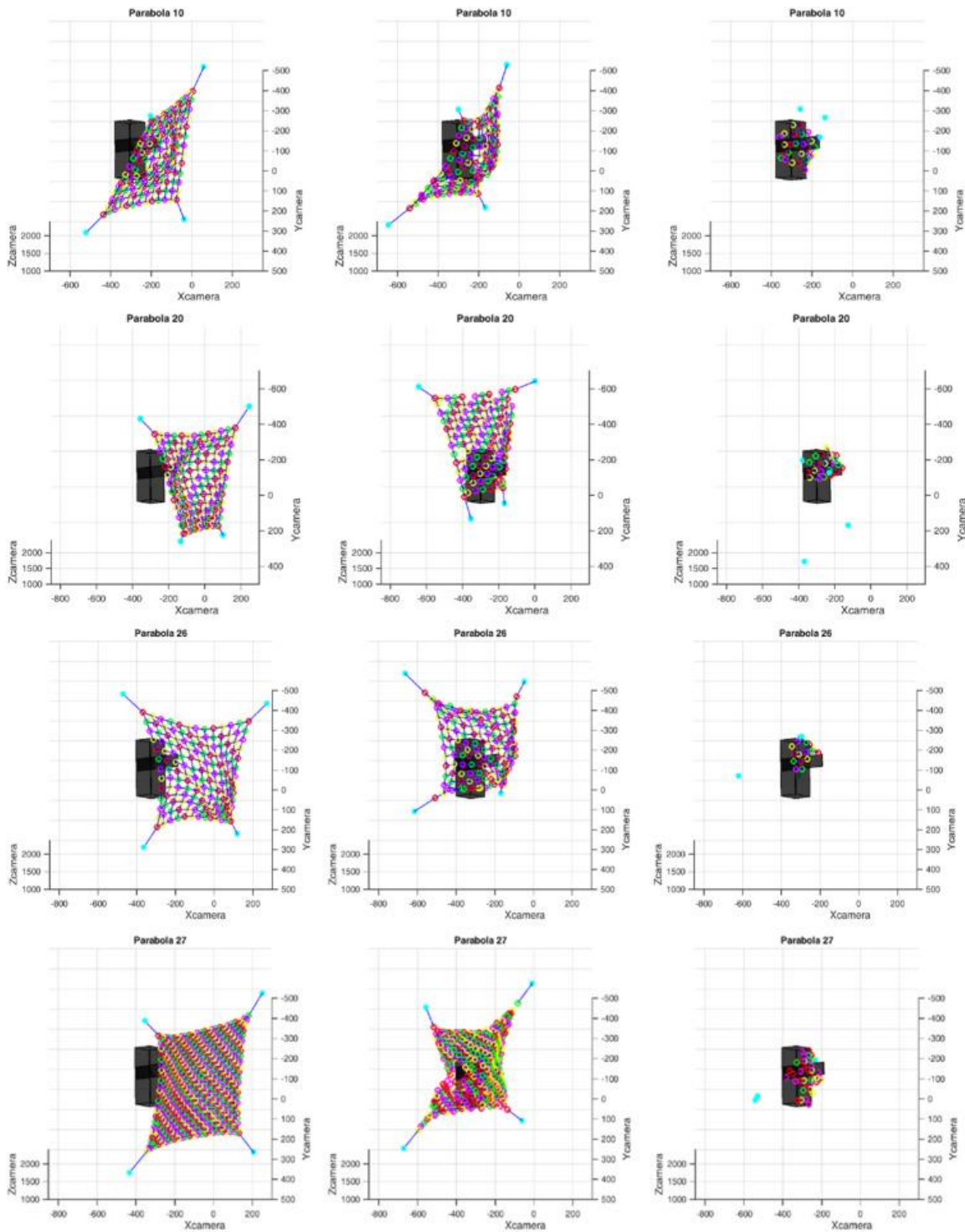
Fig. 21. First, intermediate and final 3D reconstructed net during parabolas 10, 20, 26 and 27.

5. Thrown-net simulator validation

The PATENDER Simulator has been validated from the comparison of the simulation data and the data obtained from the 3D reconstruction of the parabolic flight experiment images. The validation process was initially considered to be performed through the direct comparison between the positions of the simulated particles and the reconstructed particles. However, after the large experience and know-how acquired on the dynamics involved in the net wrapping process, the positions comparison approach is stated as insufficient since it is not considering enough

information. After a first investigation of the process, three phases with different physical characteristics have been clearly identified:

- Net free-flight deployment. This free-flight phase starts with the net fully deployed and finishes with the first contact over the target mock-up. It is dominated by the net internal dynamics considering the tensions involved during the net links elongation process. For almost all parabolas this first phase is empty since the net is colliding in the parabolic-flight experiment since the first reconstructed frame. Only during the parabola #10, five frames (out of a total of 200 frames) correspond to this phase; all other 3D reconstruction process start with the net directly colliding against the target within the first reconstructed frame. This lack of frames during this phase #1 is due to difficulties experienced during the execution of the parabolic flight experiment. During the parabolic flight it was required to increase the initial launch velocity as not all bullets were being shoot simultaneously (much more found friction within the bullet liners found than expected). Besides this it was generated some motion blur over the acquired images reducing the quality of the 3D reconstruction. Furthermore, the 3D reconstruction was developed requiring a full deployment of the net before hitting the target and this constraint was also reducing the number of frames during this free-flight phase.

This phase is well explained by the theoretical equations described in [10]. Initial errors in the positioning or attitude will introduce an error offset in the propagation of the system while initial errors in the linear velocity or angular rates will imply constant error increments (as shown in Fig. 22-a below). During this phase a direct comparison of particles between results from the simulator and the 3D data reconstructed through normalized absolute differences of bullet positions has been determined enough to validate the performances of the simulator.

- Initial wrapping of the target. This phase starts after the first collision of any net particle (e.g. first contact of the net with the frontal part of the target mock-up) against the target. During this phase the contact dynamics is adding additional reaction forces between the net particles and the target. Such collisions are not properly captured by the simulator as infinitesimal difference on the initial conditions are producing completely different results; for example, small differences on the bullet attitude and position produce completely different scenarios for the net dynamics propagation. In order to validate the simulator the bullet positions comparison is considered not enough and additional metrics based on the net shape are included:

    a. Dispersion index (Boyce-Clark, 1964) [15] as averaged distance from the centroid of a shape to all points on the shape perimeter. This index calculates very quickly the compactness of a shape using only the points in the perimeter. It is considered as a basic metric for cases where an average spread of a phenomena is considered of interest (as in the case of the net wrapping around the target).
    b. Convex hull volume as the convex polygon with the shortest possible perimeter that fully encompasses the shape. This feature is deemed appropriate when the shape is an obstacle to passage and cannot be traversed. In our scenario the obstacle is the target mock-up to be captured; the full wrapping of the net implies that the net shape is similar to a rectangle and the absence of spikes is similar to the final configuration where the knots from net to bullets are fully over the target and not anymore flying around the target.
    c. 3D moments order 1 and order 2. These 3D moments measure the spatial distribution of 'mass' or voxels of a shape. They are invariant to translation and rotation. We have been using the equations proposed within the 3D Point-cloud library [16], [17]. Such two moments are normalized by the Point-Cloud zero moment in order to get them invariant to scale changes.
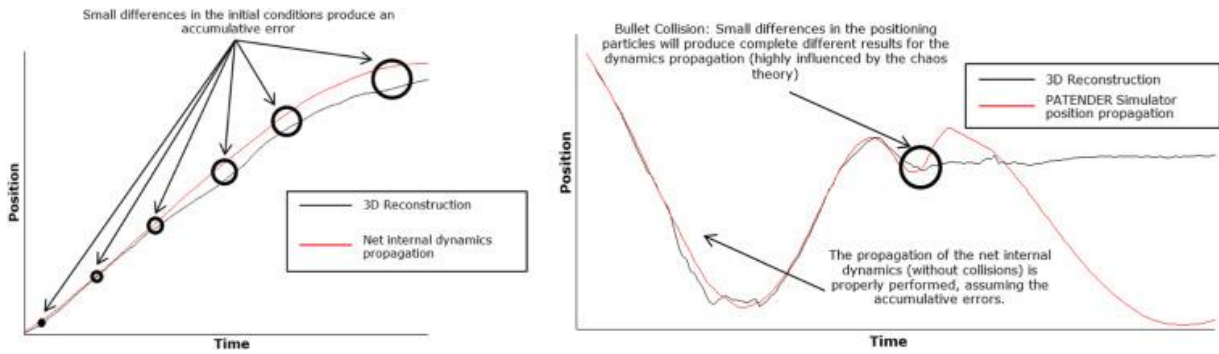
Fig. 22. Accumulative errors generated during the propagation of the net internal dynamics (left) and propagation of errors after first bullet collision (right).

The dispersion index and the convex hull volume are metrics easy to be evaluated as shown in Fig. 23 below, since both of them are related to simple concepts and units.

- Full wrapping of the target. This phase starts whenever we have a first collision of all four bullets against themselves, the target and the target arm holder. During this phase all the particles are highly influenced by chaotic effects since many collisions start to occur (several examples are shown in Fig. 24 below). For this reason, the comparison based on particles position is not valid anymore and hence, for this phase we only rely on the comparison of the previously mentioned shape features.
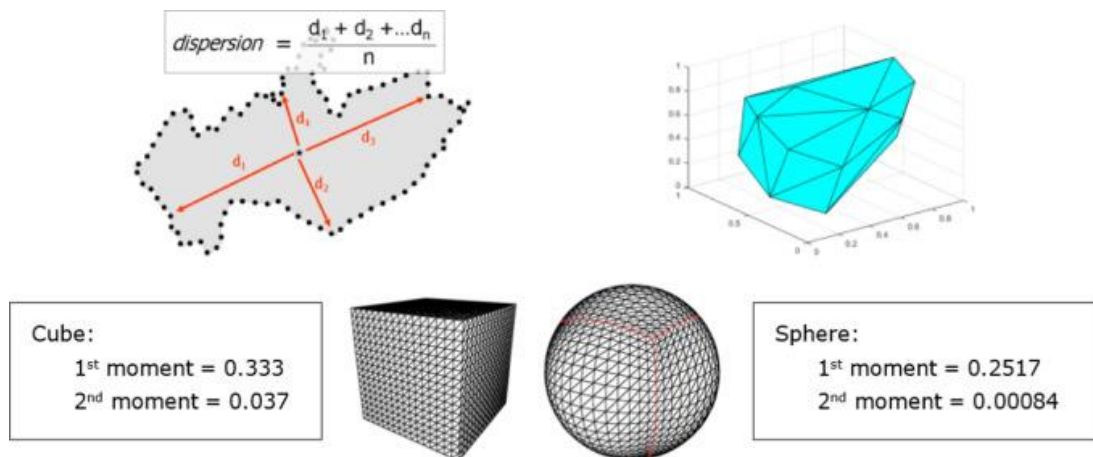

Fig. 23. Proposed comparison metrics. From left to right: dispersion index, convex hull volume and first and second order 3D moments for a cube and a sphere.
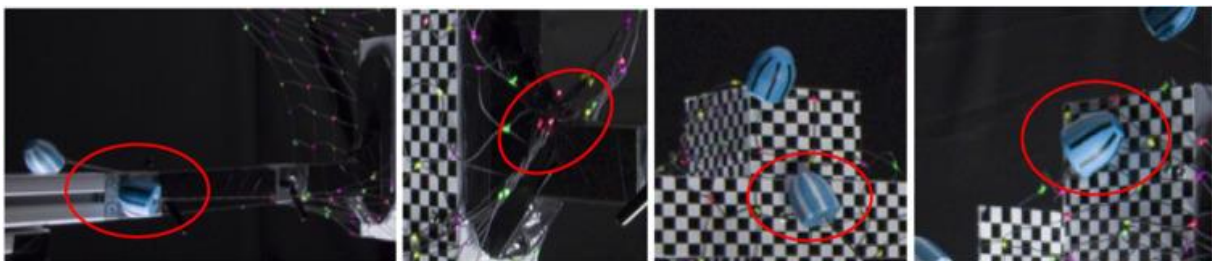

Fig. 24. Example of collisions between bullets and target mock-up elements (arm holder, rear side, frontal antenna and lateral side).

5.1. Bullets and knots positioning differences

Fig. 25 below shows the knots and bullets absolute position differences between simulated and 3D reconstructed data from parabola #17. It is clearly shown that after first bullet collisions (around t=0.5 s) the bullet positioning errors start to increase dramatically (reaching maximum error values of 0.4 m of similar size to the net corresponding size of 0.6×0.6 m). By restricting the differences to the net knots we compute an averaged mean positioning difference of 30 mm during the first phase and 15 mm during the final wrapping phase (meaning a 2.5% error with respect to the net size). Individual knots positioning errors stay below 30 mm during such phase (5% error of the net size).
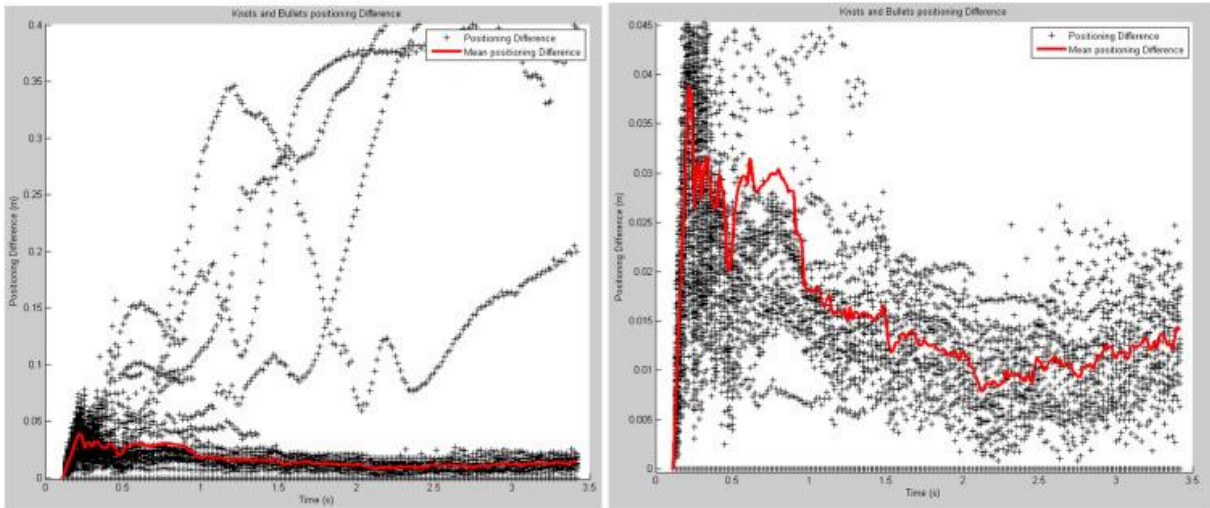

Fig. 25. Knots and bullets absolute position differences between simulated and 3D reconstructed data: overall overview including bullets (left) and zoomed view restricted to knots differences (right).

A closer look to the positioning of bullets #1 and #2 during the parabola #17 is presented by Fig. 26. On the left side of the figures it is shown the XYZ position of bullet #1 (simulated position on the black line and 3D reconstructed position on the red line) and on the right side the scaled absolute differences of XYZ position of bullet #1 between simulated and 3D reconstructed positions. The initial wrapping phase is highlighted in blue colour while the final wrapping (full wrapping of the target) phase appears under a yellow colour background.
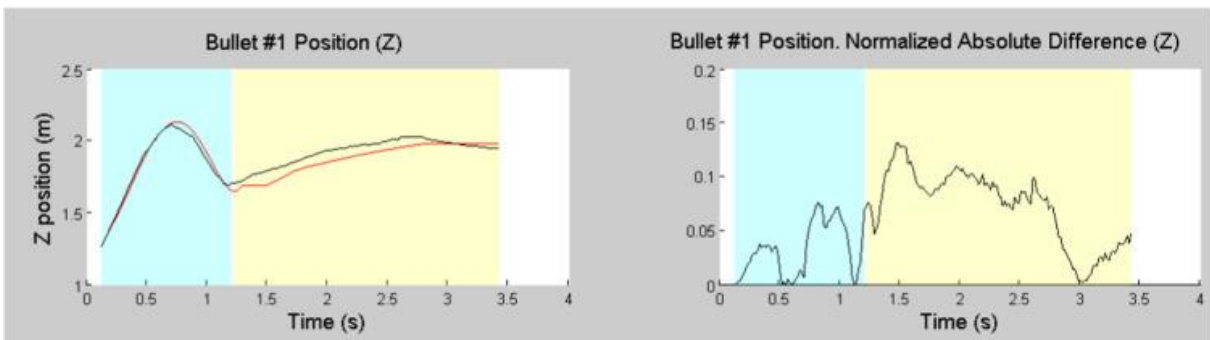

Fig. 26. Parabola #17. Z Positioning of bullet #1.

The comparison of the bullet positions is not considered suitable to be performed through a relative difference metric since the bullet position values for components X and Y will cross over zero position (relative difference is not defined for zero reference value, and provides useless results for

reference values near to zero). In order to use a scale invariant metric, the absolute difference is scaled with the net size (0.6 m of net size +0.15 m of bullet link length).

It is shown that the XYZ trajectory of bullet #1 (upper left bullet) is very similar from the simulator to the 3D reconstruction up to the end of the initial wrapping phase. Later on, at time t~1.2 s the bullet #1 collides and both curves start diverging. Looking at the scaled absolute differences graph it is shown that during the initial wrapping the maximum error is below 10% while during the final wrapping the error grows up finalizing with an error of 80% of the net size in the Y direction.

By visually comparing the absolute positioning differences of bullet #2 (upper right bullet), we can conclude, that during the initial wrapping phase, the simulator is able to follow the 3D reconstructed positions. During the final wrapping phase, the simulated positions start to diverge from the 3D reconstructed ones (12.2% of error for 3-sigma deviation as average error from all 4 bullet XYZ positions).

5.2. Dispersion index and convex hull volume

The dispersion index comparison is shown in Fig. 27 (left) below. In these graphs it is shown that the relative difference for the dispersion indices has peak values of 6% during the initial wrapping with an averaged error of 3% and a final error of 4% for the final wrapping. This error is clearly produced by an offset between simulated and reconstructed dispersion indices; both curves are following each other offering the same evolution over the time.
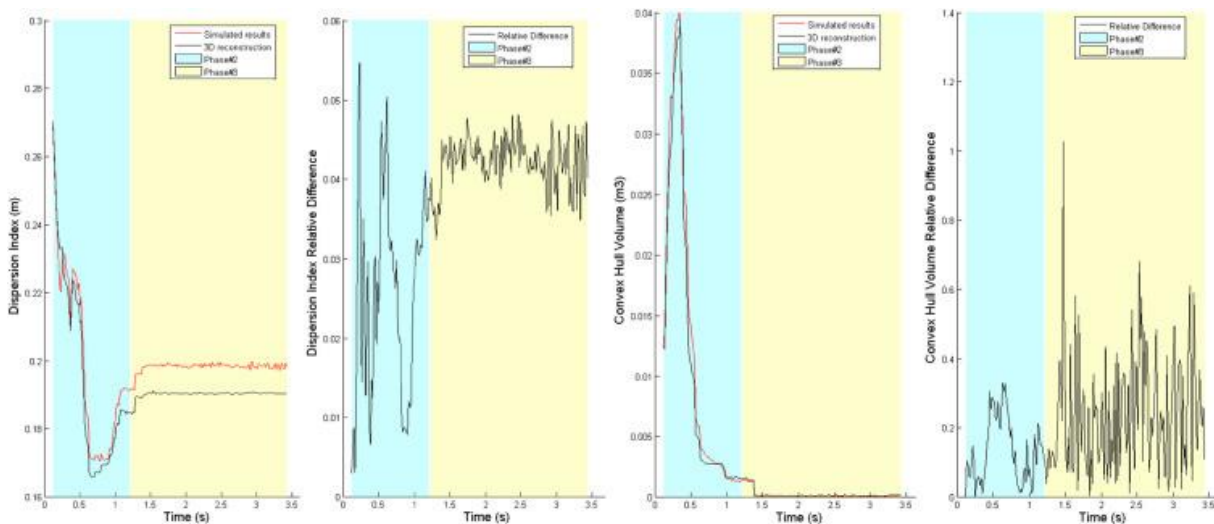

Fig. 27. Parabola #17 - Comparison between simulated and 3D reconstructed results: dispersion index (left) and convex hull volume (right).

Similar results are reported within Fig. 27 (right) by the comparison of the convex hull volumes. Initially the relative difference is about 10% with a peak value of the 25% finalizing with an error of 17%, also considered as an offset error (it is kept very constant during the whole final wrapping phase). Mentioned offset errors are considered a scale difference because they are not present in the computed 3D invariant moments.

5.3. 3D moments of order 1 and order 2

Fig. 28 below shows the 3D point-cloud moments of zero-order, first-order and second-order. The first-order and second-order moments are normalized with zero-order to obtain translation, rotation and scale invariant moments. For this reason, the absolute difference metric is not reported for the zero-order moment (the zero-order moment is not scale invariant). It is observed that the simulated

overall net shape is very similar to the reconstructed one during the experiment. The absolute difference between both curves presents a peak/median error of 0.012/7e-4 for the first order 3D moment and of 5e-3/3e-4 for the second order 3D moment as shown in Table 3 below. By comparing the median error against the corresponding 3D moments of a cube (as typical shape similar to the target mock-up), we are obtaining percentage errors of 0.23% and 0.78% for the 3D moments of order 1 and 2.
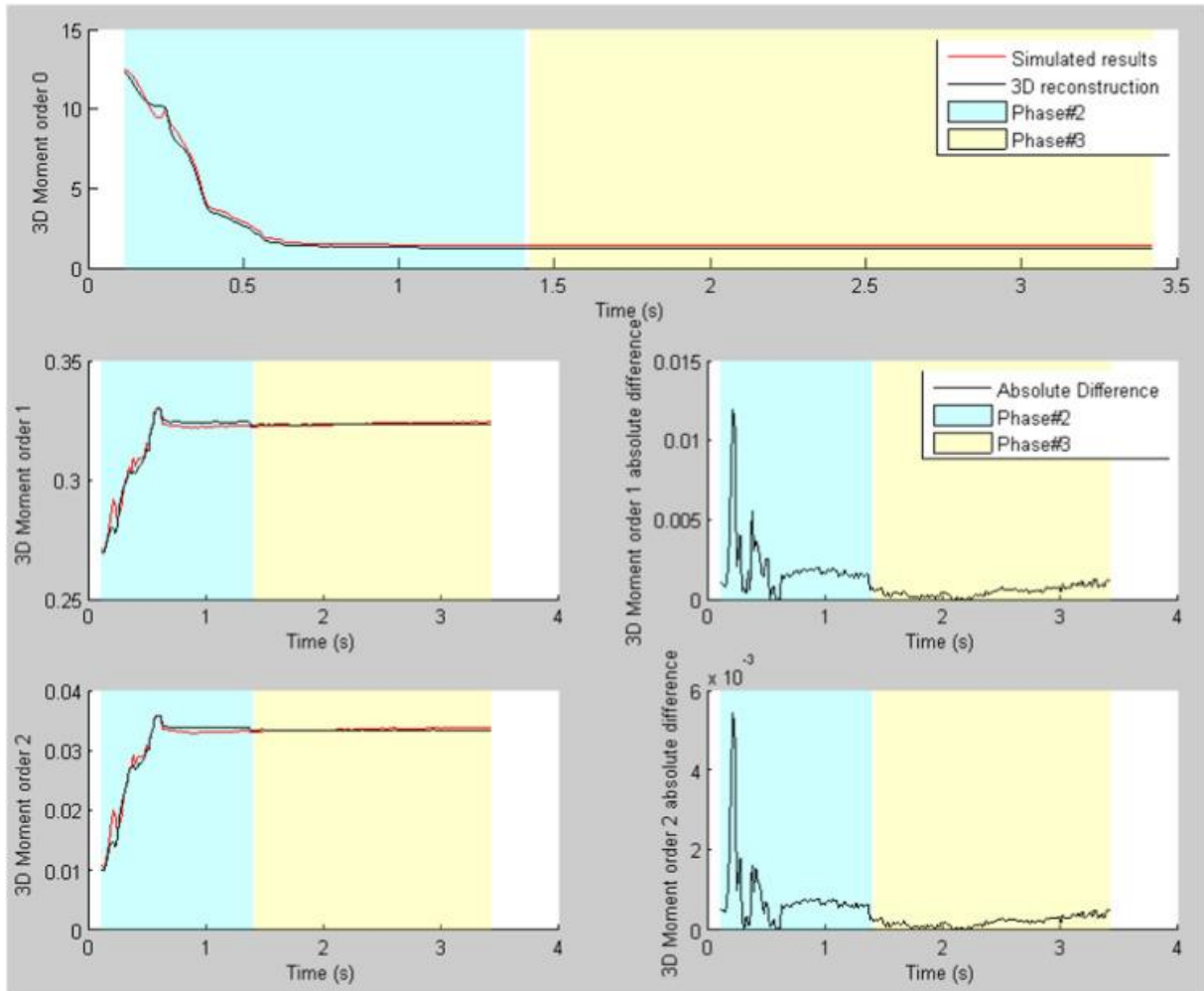

Fig. 28. Parabola #17 - Comparison of 3D moments order 0, 1 and 2 (simulated and 3D reconstructed results).

3D Moment	Cube 3D moment	Peak error	Mean error	Median error	Average error (% median over cube 3D moment)
First moment	0.333	0.012	0.00115	0.00077	0.23%
Second moment	0.037	0.005	0.00048	0.00029	0.78%

Table 3. Parabola #17. Comparison of 3D moments against corresponding cube shape.

As previously described during the comparison of the dispersion index and the convex hull volume features, the error offset in the invariant moments is negligible and this allows it to be considered as an error offset.

5.4. Overall comparison

Fig. 29, Fig. 30 and Fig. 31 below show an overall comparison of dispersion indexes, convex hull volumes and 3D moments absolute differences between simulated and 3D reconstructed results for parabolas #10, #20, #26 and #27. In both cases (dispersions indexes and convex hull volumes) the curves are having the same trend finalizing in an almost constant error. In the case of 3D moments, it is shown that some peak errors appear during the initial wrapping phase (in blue colour) and are reduced very much during the final wrapping phase (in yellow colour).
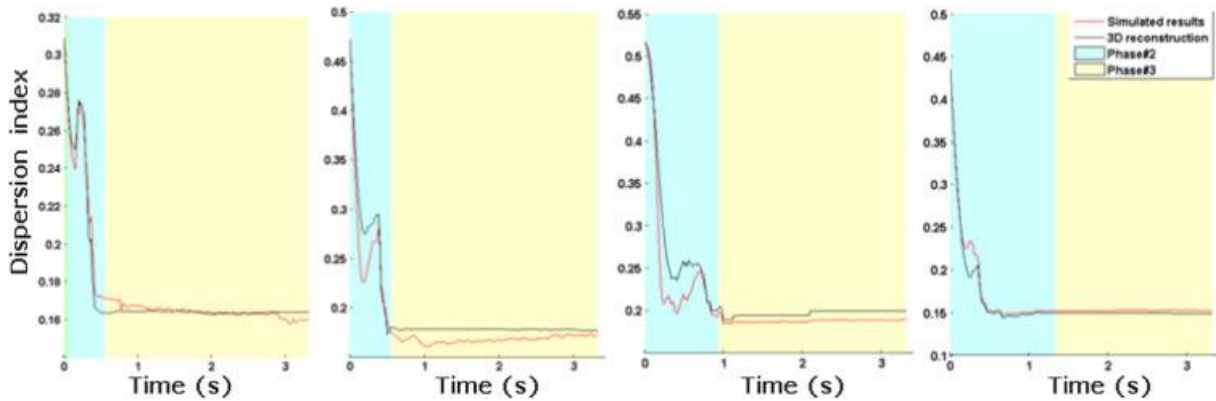

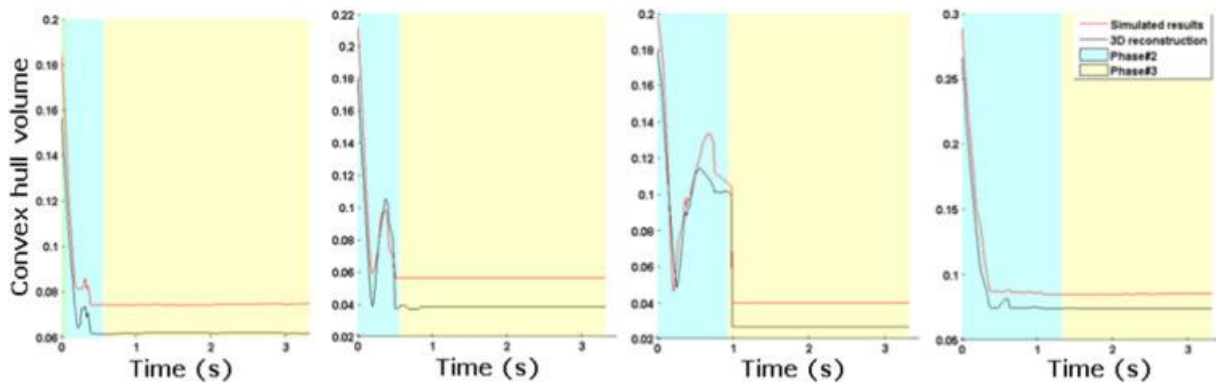Fig. 29. Comparison of dispersion indexes (parabolas #10, #20, #26 and #27).

Fig. 30. Comparison of convex hull volumes (parabolas #10, #20, #26 and #27).
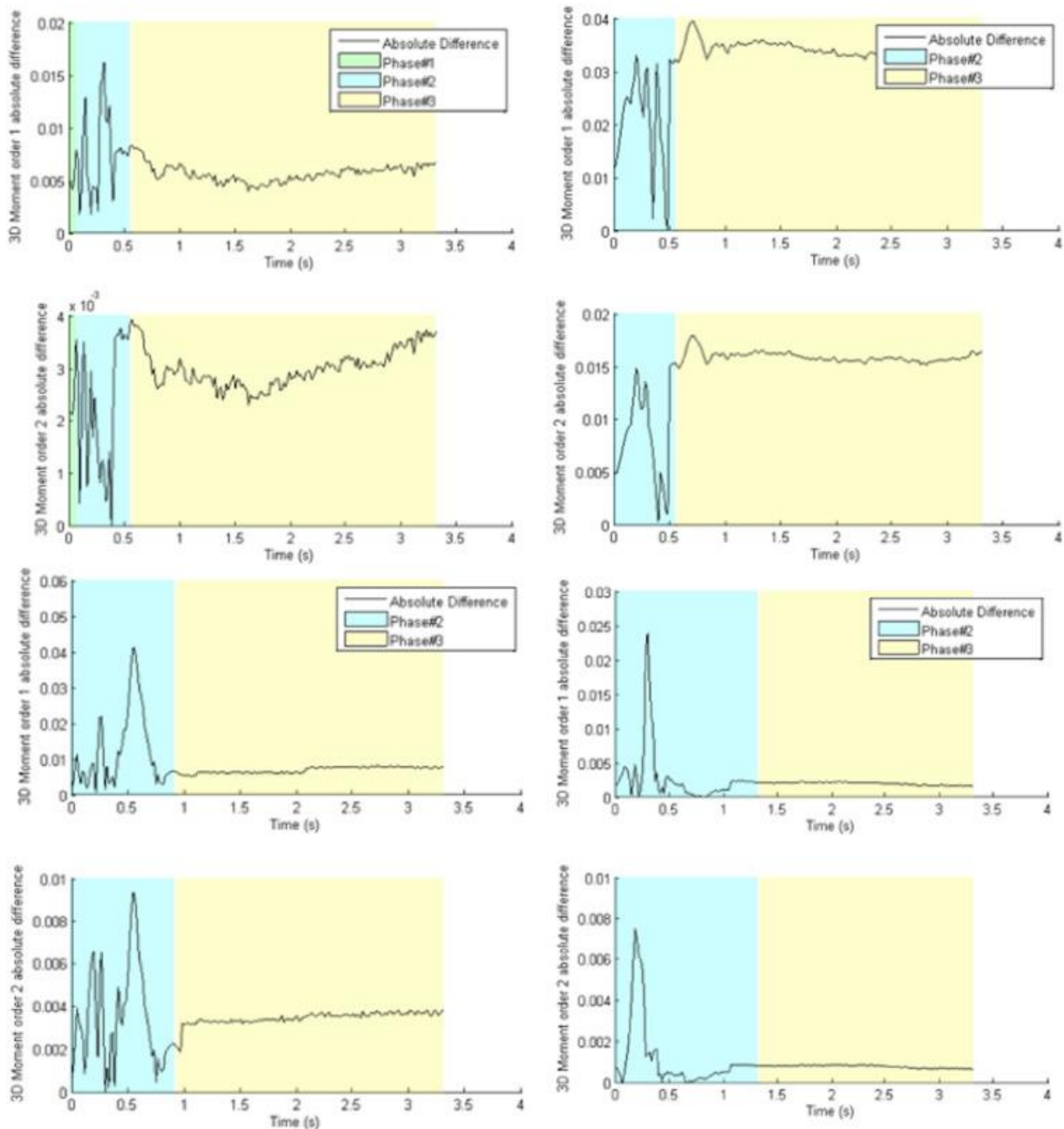
Fig. 31. Comparison of absolute differences between simulated and 3D reconstructed results from 3D moments of order 1 and order 2 (parabolas #10, #20, #26 and #27).

Finally Table 4 and Table 5 below present an overall overview of the mean absolute positioning differences of bullets, relative difference of dispersion indexes and convex hull volumes and 3D moments order 1 and order 2 between simulated and 3D reconstructed results. The 3D moments are compared trough absolute differences. It has also been performed a cross-validation exercise against one set of parabolic data extracted from the AdriNet activity [5] (but not taken into account into the final statistics; computed indexes are slightly above defined pass-fail criteria and this is most probably due to not proper definition of the initial conditions). The comparison between validation metrics allows to extract the following conclusions:

During the initial wrapping phase the bullets positioning differences are around 11.5% with a low standard deviation of 3.5% with similar values with respect to the convex hull volume (as this volume is mostly affected by the bullets positioning). In this phase the dispersion index provides a more reduced relative difference.

During the final wrapping phase the mean dispersion index decreases down to the 3% with a low standard deviation between parabolas. The convex hull volume relative differences are not considered a good metric as it is affected by an error offset observed at the beginning of this phase. In this phase the 3D moments of order 1 and order 2 provide only a 2.3% and 12% of error with respect to the corresponding 3D moments of a similar cube shape.

Parabola Number	Mean Abs. Diff. Bullet Positions [%]	Dispersion index relative difference [%]	Convex hull volume relative difference [%]
17	9.48	6	24.6
10	12.00	4.5	21
11	12.31	2.9	3
16	7.58	7.2	10
18	12.15	1.5	5.8
20	19.10	3	4.8
26	6.96	4	5
27	12.51	2	15
30	7.43	7	18
SKA	30.00	7.5	20
Mean	**11.06**	**4.23**	**11.91**
Standard deviation	**3.79**	**2.11**	**7.98**

Table 4. Initial wrapping phase: Comparison of validation metrics.

Parabola Number	Dispersion index relative difference [%]	Convex hull volume relative difference [%]	3D Moment Order 1 Abs Difference [%]	3D Moment Order 2 Abs Difference [%]
17	4.2	18.5	0.10	0.04
10	2.5	20.5	0.6	0.35
11	2.7	3	0.6	0.3
16	2.2	3	0.4	0.09
18	1.8	4.8	0.03	0.028
20	2	46	3.4	1.6
26	5.3	50	0.78	0.37
27	2.8	15	0.20	0.8
30	3.0	19	1.4	0.3
SKA	30	40	2.8	1.1
Mean	**2.94**	**19.98**	**0.84**	**0.43**
Standard Deviation	**1.13**	**17.37**	**1.05**	**0.50**

Table 5. Final wrapping phase: Comparison of validation metrics.

The PATENDER simulator is considered to represent accurately the first phase of free-flying deployment. After the first collisions of the bullets against the target they appear chaotic effects and the simulator start losing representativity from the point of view of RMS comparison of bullets and knots positions; during this initial and full target wrapping phases the validation of the simulator has been performed using shape features such as the dispersion index, the convex hull volume and the first and second 3D point-cloud moments (as the overall shape of the net is still kept during these phases); further efforts should be directed to refine this shape analysis and comparison.

6. Conclusions

The PATENDER experiment was flown within the Novespace parabolic flight experiment VP116 of June 9th, 2015 where microgravity conditions were reached during some few tens of seconds (in fact the experiment preparation, net launching and capturing of the target mock-up was done in around 10 s). All the parabolas were used to test different net configurations and deployment angles. Several nets were launched using a pneumatic-based dedicated mechanism in order to represent the capture of large space debris. The parabolic flight experiment was designed to maximize the probability of successful wrapping, by tuning net shooting velocity/angle and target position. More than 76% of successful deployments and wrapping were obtained during the flight campaign. After screening the parabolas with enough quality for the 3D reconstruction process, a total of 9 parabolas have been analysed. Future ADR experiments within parabolic flights are recommended to consider lower launching velocities and an automatic triggering of the launch whenever the residual 0-g microgravity of the parabola initiated by the aircraft is close to zero.

The 3D reconstruction process has been very laborious requiring manual tracking of some elements such as the bullets. Furthermore, a graphical user interface was developed to help the user processing the images manually (allowing to insert missed points and remove false positives). The colour segmentation step was properly performed after insertion of a background subtraction to eliminate from the image spurious points and light flares from the image (the images acquired were disturbed by led light's creating colours on racks and other items with their reflections therefore creating false positives).

The PATENDER simulator has been configured with the experiment performed during the parabolic flight including the net topology, the net material parameters and the state for all the particles (position, attitude and rates for the target mock-up, net knots and net launcher). During the initial frames, the simulator was able to propagate the complex dynamics involved in the system. The estimated positions of the net particles have been statistically compared with the data obtained from the 3D reconstruction providing accurate results for all the parabolas reconstructed.

After the first contact of the net against the target it has been observed that the bullets positioning differences between the simulation and the 3D reconstruction increase drastically at specific time events. These time events have been identified in the raw images as a result of collisions performed by some elements of the net. Such collisions imply that the dynamics of the whole system starts to be affected by the chaos theory. Due to this reason, new shape metrics have been researched to validate the simulator, as the overall shape of the wrapped net is still possible to be compared between simulation and 3D results. The shape dispersion index and convex hull volume metrics allow to validate the results of the simulator during this initial wrapping phase.

During the final wrapping phase the shape metrics features have less variations because the target has been fully wrapped and the velocity of the bullets significantly reduced. In the case of the 3D moments metric it is shown that the final error is much reduced and the net shape determined by the simulator is very similar to the 3D reconstructed results (also demonstrated for one set of 3D reconstructed data extracted from the AdriNet activity [5]).

Subsequent phases of a de-orbit operation such as the pulling of the wrapped target mock-up with a tether system were not considered within the scope of the activity and they are foreseen as future continuation works. The increase of the TRL level of the simulator could be further achieved by an in-orbit experiment based on a sounding rocket.

References

1. Euroconsult, Satellites to be Build & Launched by 2024 Report. August. Reference WS315, 2015.
2. J.C. Liou, N.L. Johnson, Risks in space from orbiting debris, Science, 311 (5759) (2006), p. 340

3. K. Wormnes, R. Le Letty, L. Summerer, R. Schonenborg, O. Dubois-Matra, E. Luraschi, A. Cropp, H. Krag, J. Delaval, ESA technologies for space debris remediation. in: Proceedings of the 6th European Conference on Space Debris, Darmstadt, 2013.
4. M. Dyrek, Z. Derda, W. Golebiowski, Stereographic system for reconstruction of net flight trajectory, ESA ASTRA 20015.
5. W. Gołębiowski, R. Michalczyk, M. Dyrek, U. Battista, K. Wormnes, Validated simulator for space debris removal with nets and other flexible tethers applications, Acta Astronaut., 129 (2016), pp. 229-240
6. E.M. Botta, I. Sharf, A.K. Misra, M. Teichmann, On the simulation of tether-nets for space debris capture with vortex dynamics, Acta Astronaut., 123 (2016), pp. 91-102
7. M. Shan, J. Guo, E. Gill An Analysis of Critical Deployment Parameters for Tethered-Net Capturing for Space Debris Removal. 66th International Astronautical Congress (IAC 2015); 2015 12–16 October; Jerusalem, Israel.
8. J. Forshaw, et al., Remove DEBRIS: an in-orbit active debris removal demonstration mission, Acta Astronaut., 127 (2016), pp. 448-463, (ISSN 0094-5765)
9. R. Benvenuto, M.R. Lavagna, Flexible capture devices for medium to large debris active removal: simulation results to drive experiments, ESA ASTRA (2013)
10. L. Cercós, R. Stefanescu, A. Medina, R. Benvenuto, M. Lavagna, I. González, N. Rodríguez, K. Wormnes, Validation of a net active debris removal simulator within parabolic flight experiment, i-SAIRAS (2014), (Montreal, June 2014)
11. C. Lee, B. Cha, H. Kim, Physical modelling for underwater flexible systems dynamic simulation, Ocean Eng. (2005), pp. 331-347
12. G. Hippmann, An algorithm for compliant contact between complexly shaped surfaces in multibody dynamics. IDMEC/IST, Lisbon, Portugal, July 1-4, 2003.
13. M. Pollefeys Visual 3D Modeling from Images. Tutorial Notes, University of North Carolina, USA. http://www.cs.unc.edu/~marc/tutorial.pdf
14. M. Pollefeys, L. Van Gool, M. Vergauwen, F. Verbiest, K. Cornelis, J. Tops, R. Koch, Visual modelling with a hand-held camera, Int. J. Comput. Vis., 59 (3) (2004), pp. 207-232
15. R.R. Boyce, W.A.V. Clark, The concept of shape in geography, Geogr. Rev., 54 (1964), pp. 561-572
16. 3D Moments (j1, j2, j3) computation – Point Cloude Library (PCL) v1.8.0: http://docs.pointclouds.org/trunk/classpcl_1_1_moment_invariants_estimation.html.
17. R. Bogdan, S. Cousings, 3D is here: Point Cloud Library (PCL), IEEE ICRA, May 9-13, 2011.